








## Selective manipulation and tunneling spectroscopy of broken-symmetry quantum Hall states in a hybrid-edge quantum point contact

Wei Ren <sup>1,\*</sup>, Xi Zhang <sup>1,\*</sup>, Jaden Ma <sup>1</sup>, Xihe Han <sup>2,3</sup>, Kenji Watanabe <sup>4</sup>, Takashi Taniguchi <sup>5</sup>, and Ke Wang <sup>1,†</sup>

<sup>1</sup>*School of Physics and Astronomy, University of Minnesota, Minneapolis, Minnesota 55455, USA*

<sup>2</sup>*Department of Physics, University of Wisconsin, Madison, Wisconsin 53706, USA*

<sup>3</sup>*Department of Physics, The Ohio State University, Columbus, Ohio 43210, USA*

<sup>4</sup>*Research Center for Electronic and Optical Materials, National Institute for Materials Science, 1-1 Namiki, Tsukuba 305-0044, Japan*

<sup>5</sup>*Research Center for Materials Nanoarchitectonics, National Institute for Materials Science, 1-1 Namiki, Tsukuba 305-0044, Japan*



(Received 26 July 2023; revised 10 October 2023; accepted 20 November 2023; published 22 December 2023)

We present a device architecture of hybrid-edge and dual-gated quantum point contact. We demonstrate improved electrostatic control over the separation, position, and coupling of each broken-symmetry compressible strip in graphene. Via low-temperature magnetotransport measurement, we demonstrate selective manipulation over the evolution, hybridization, and transmission of arbitrarily chosen quantum Hall states in the channel. With gate-tunable tunneling spectroscopy, we characterize the energy gap of each symmetry-broken quantum Hall state with high resolution on the order of  $\sim 0.1$  meV.

DOI: [10.1103/PhysRevB.108.245423](https://doi.org/10.1103/PhysRevB.108.245423)

### I. INTRODUCTION

Electronic states in graphene exhibit a fourfold spin-valley degeneracy [1–6], which can be lifted with an external magnetic field [7–18]. The broken-symmetry quantum Hall edge states (QHES) can carry spin- and valley-polarized currents. Proper manipulation of these currents can serve as a basis for advanced device platforms with rich quantum physics including topics such as Mach-Zehnder interferometry [19,20], the quantum spin Hall effect [21–24], and topological superconductivity, towards utilizing them for future quantum electronics and computing platforms. Accurate determination of energy gaps between degeneracy-lifted Landau levels (LL) and their dependence on disorder and local electrostatic fields can also shed new light on the microscopic details of the QHES.

Previous experiments have demonstrated control over the transmission of QHES via a macroscopic gated region [25] or a mesoscopic quantum point contact (QPC) [26–28]. The former scheme allows selective filtering of broken-symmetry states but lacks continuous tunability for its transmission (either 0 or 1). The later scheme allows partially reflected/transmitted quantum Hall (QH) states, but the relatively abrupt electrostatic profile makes it difficult to separate the coexisting broken-symmetry QH states into well-isolated compressible strips for precise and selective manipulation. Recent advancements have addressed some of these challenges by enhancing the quality of graphene QPC devices. Broken-symmetry QHES have been observed in split-gated graphene QPC devices with split gates [29], and manipulation of fractional quantum Hall states has been achieved in QPCs

defined by graphite gates [30,31]. Notably, quantum Hall interferometry in graphene, relying on high-quality QPCs, has been successfully demonstrated in both the integer quantum Hall regime [30] and the fractional quantum Hall regime [32].

In this work, we demonstrate a type of hybrid-edge and dual-gated QPC, whose boundaries are defined by a physical edge, and a tunable  $pp'$  or  $pn$  interface from independently gated regions. The device is “hybrid edge,” with the left (right) boundary of the QPC being the physical (electrostatically defined) edge of graphene. By tuning the QH edges states closer to the physical (electrostatic) edge with an abrupt (smooth) spatial profile, the separation and coupling of the edge states can be precisely manipulated by demand. The device is “dual gated,” with electrostatics inside the QPC codefined by a pair of local nanogates and a global bottom gate. This allows more versatile and precise electrostatic control over the location, transmission, and tunneling of selected QHES.

The unique device operation scheme is capable of more adiabatic and selective control over the emergence, evolution, location, transmission, and width of broken-symmetry edge state for gapless materials such as graphene. We show that the improved level of control enables selective and tunable tunneling spectroscopy of QH states, similar to that of Coulomb blockade, allowing precise measurement of QH gaps with high-energy resolution without relying on variable temperature measurements. This is especially relevant for symmetry-broken states or emergent correlated states (in moiré systems), where interaction-driven gap can be temperature dependent.

A pair of atomically flat metal split gates [Fig. 1(a)] is deposited onto a 285-nm layer of  $\text{SiO}_2$  grown on top of a  $p$ -doped silicon substrate. An hBN-encapsulated monolayer graphene stack is then transferred on top of the gates and etched into a “Λ” shape with the sample edge aligned with the gate boundaries (see Supplemental Material, S1) [33].

\*These authors contributed equally to this work.

†kewang@umn.edu

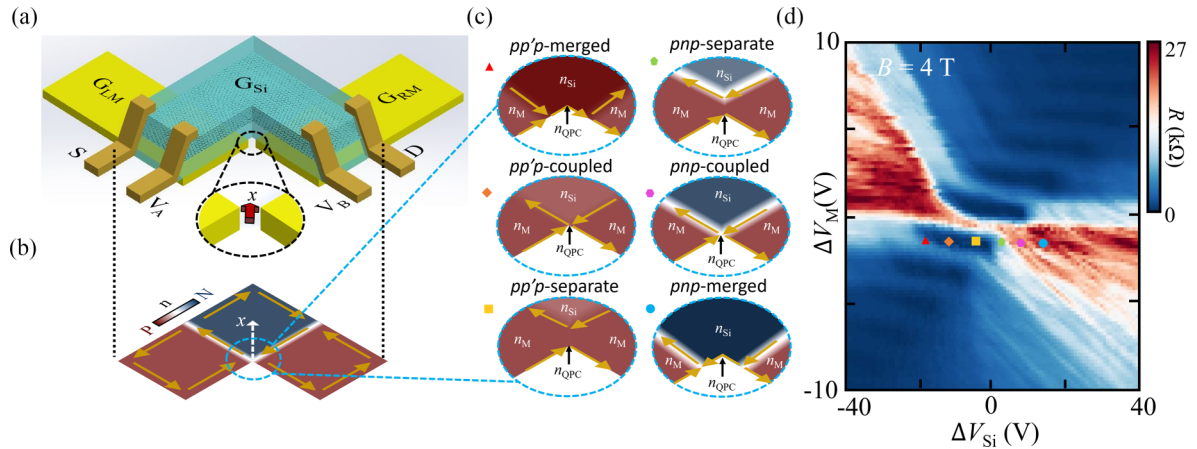


FIG. 1. Gate-tunable quantum point contact. (a) Schematic of the device. The sample can be electrostatically defined into three regions, whose carrier densities are control by the metal gates ( $G_{LM}$  and  $G_{RM}$ ) and silicon backgate ( $G_{Si}$ ), respectively. Inset: Zoom-in on the QPC. The red arrow indicates the direction of  $x$ . (b) Corresponding carrier-density distribution. The blue and red colors represent the  $n$ -type and  $p$ -type carrier density. (c) Carrier-density distribution in the region near the QPC channel, at six typical configurations. The doping in center of channel ( $n_{QPC}$ ) is simultaneously determined by the fringing field from  $G_{LM}$ ,  $G_{RM}$ , and  $G_{Si}$  from beneath the gate separation. (d) Measured four-probe resistance as a function of voltage applied with respect to charge neutrality,  $\Delta V_M$  and  $\Delta V_{Si}$  at  $B = 4$  T.

The left/right metal gates ( $V_{LM}/V_{RM}$ ) and the silicon backgate ( $V_{Si}$ ) independently tune the carrier density of the corresponding device region above, while competing in determining the carrier densities at region boundaries ( $n_{QPC}$ ). The measurements are conducted in a  $3\text{He}/4\text{He}$  dilution refrigerator at a base temperature of  $\sim 10$  mK. The four-probe resistance is measured by applying an alternating current of 100 nA through the source and drain contacts and measuring the voltage difference between two additional contacts across the device (see Supplemental Material, S1 for more detailed discussion). By applying an out-of-plane magnetic field  $B$ , a 1D constriction is created near the mutual edge of all three device regions [Fig. 1(b)]. The electrostatics near this critical device region benefits from several elaborate experimental designs distinctive from conventional gate-defined QPCs. This allows precise control over QHES in the channel via an “L”-shaped electrostatic profile (see Supplemental Material, S2) [33].

## II. GATE-TUNABLE QUANTUM POINT CONTACT

The doping of the channel is cocontrolled by all three gates, allowing more versatile and precise control inside the channel. The width of the channel is tuned by fringing-field defined QPC, with a tunable smooth electrostatic profile for spatial separation/isolation of QHES. Figure 1(c) illustrates the carrier-density distribution in the device for six typical configurations of QHES in the channel, each demonstrated by and corresponding to a marked data point in measured four-probe resistance as a function of  $\Delta V_M$  and  $\Delta V_{Si}$  at  $B = 4$  T [Fig. 1(d)].  $V_M \equiv V_{LM} = V_{RM}$  denotes the same gate voltage applied to both metal gates, and  $\Delta V_M = 0$  ( $\Delta V_{Si} = 0$ ) defined at when the region above gate  $V_M$  ( $V_{Si}$ ) is charge neutral (zero carrier density). As the difference between the carrier density in the metal-gate region,  $n_M$ , and the carrier density in the backgate region,  $n_{Si}$ , becomes larger, the channel width decreases. The QH states on two hybrid boundaries of the

channel are completely merged (separated) when  $|n_M - n_{Si}|$  is sufficiently large (small). This leads to quantized fractional conductance (zero longitudinal resistance), typical for pnp junctions (Hall bars) [48,49]. At the transition between the merged and separated regimes, the counterpropagating or copropagating QHES at the two boundaries of the QPC are tunnel coupled. In this “coupled” regime, the emergence, position, coupling, transmission, and evolution of the QHES can be precisely controlled in the device. It is important to note that conductance quantization is not expected with this device operation scheme, due to the hybridization of edge states at the  $pn$  and  $pp$  interface near the channel [48].

## III. SELECTIVE MANIPULATION OF BROKEN-SYMMETRY QUANTUM HALL STATES

We first tune the QPC near the coupled regime while the channel and backgate regions are of the same carrier type. This corresponds to QHES copropagating at the two boundaries of the channel. Figure 2(b) shows the measured resistance as a function of  $\Delta V_{Si}$  and  $B$  with the metal-gate voltages kept constant ( $\Delta V_M = -1.75$  V). For a given  $B$ , changes in  $\Delta V_{Si}$  simultaneously tune the width and doping of the channel. Increasing  $|\Delta V_{Si}|$  results in a larger difference in carrier density between the channel and the backgate region. This increases the penetration of the fringing field into the channel, reducing the channel width. At small (large)  $|\Delta V_{Si}|$ , the channel is wide (narrow) enough to enter the separated (merged) regime, and the measured resistance is zero (large). In the separated regime, the filling factors are  $\nu_{QPC} = -2$  for the channel (as well as the metal-gate region) and  $\nu_{Si} = -6$  for the backgate region (light-blue hexagon marker), and for the merged regime,  $\nu_{QPC} = \nu_{Si} = -6$  (golden square marker).

The  $\Delta V_{Si}$  fringing field also directly competes with  $\Delta V_M$  in determining the carrier density in the QPC,  $n_{QPC}$ , while  $n_M$  remains unchanged. As  $|\Delta V_{Si}|$  increases towards the merged regime,  $\nu_{QPC}$  evolves from  $-2$  to  $-3$ , from  $-3$  to  $-4$ , from

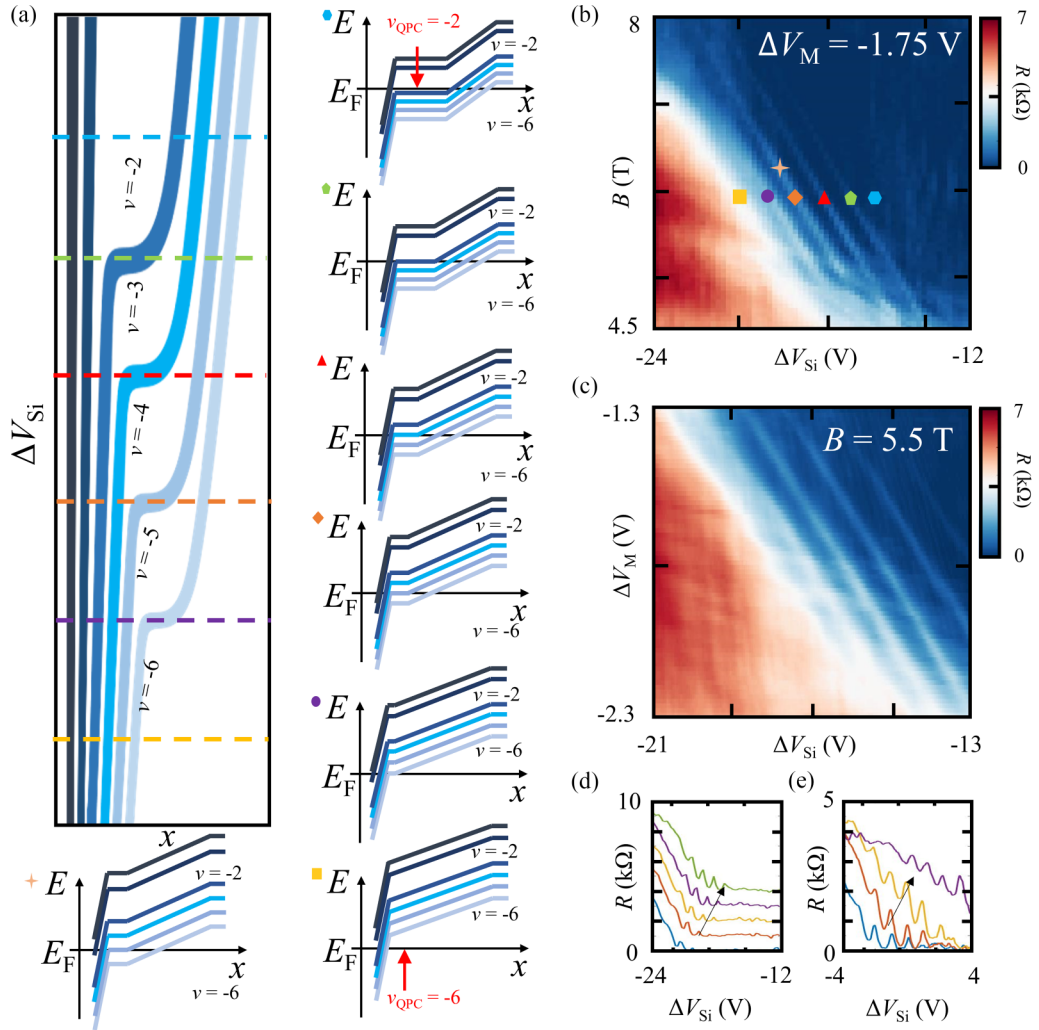


FIG. 2. Selective manipulation of broken-symmetry quantum Hall states at  $pp'p$  configuration. (a) Schematics of the evolution of spatial distribution (denoted by coordinate  $x$  along the width of QPC) of QH states in the QPC channel as  $V_{Si}$  is tuned. At certain  $V_{Si}$  values, compressible strips at channel boundary are brought to the center of the channel (color dashed line), while its corresponding Landau level brought to Fermi energy (energy-band diagram with corresponding color marks). This leads to backscattering of the selected QH state, giving rise to resistance peaks observed in (b) the measured four-probe resistance as a function of  $\Delta V_{Si}$  and magnetic field  $B$  (at constant  $\Delta V_M = -1.75$  V). (c) The evolution of the resistance peaks as a function of  $\Delta V_M$  and  $\Delta V_{Si}$  at  $B = 5.5$  T. (d) Line cuts of (b) as a function of  $\Delta V_{Si}$  at various constant  $B$  field, from 6.5 to 5.5 T. (e) Line cuts of (c) as a function of  $\Delta V_{Si}$  at various constant  $\Delta V_M$  value from  $+0.2$  to  $-0.5$  V.

$-4$  to  $-5$ , and eventually to  $-6$  [Fig. 2(a)]. Each time a degeneracy-lifted LL in the channel is in resonance (colored markers) with the Fermi energy, the corresponding QHES on the electrostatic boundary moves to the center of the channel and transitions into a bulk extended compressible state. This results in selective backscattering of that particular compressible strip and a peak in the measured resistance [Figs. 2(c) and 2(e)]. Further increasing  $|\Delta V_{Si}|$  fully fills the LL, resulting in the corresponding QHES moving to the physical boundary. This measurement demonstrates the precise movement of each compressible strip from one boundary of the QPC to the other and the ability to turn on (off) the topological protection from backscattering while it is tuned to locate at the boundary (center) of the QPC. This allows selective reflection of a chosen QHES while transmitting others.

As the  $\nu = -2$  gap increases with increasing  $B$ , a higher  $p$ -type doping is needed to maintain resonance of a

degeneracy-lifted LL with the Fermi level for a given resistance peak. This leads to a shift in the position of the observed resistance peak as a function of  $B$  [Figs. 2(b) and 2(d)].

We now configure the QPC in the coupling regime while the channel and backgate region are of opposite carrier types. This corresponds to counterpropagating QHES at the two boundaries of the channel (Fig. 3). Similar to the previous case,  $\Delta V_{Si}$  simultaneously tunes the width and doping of the channel. The measured resistance is zero (large) when  $|\Delta V_{Si}|$  is small (large), as the channel is wide (narrow) enough to enter the separated (merged) regime. In particular, the separated regime corresponds to  $\nu_{QPC} = 2$  for the channel (as well as the metal-gate region) and  $\nu_{Si} = 2$  for the backgate region (light blue circle marker). The merged regime corresponds to  $\nu_{QPC} = \nu_{Si} = -2$  (red diamond marker).

The microscopic details of the coupling regime are in contrast with the previous case. As  $|\nu_{QPC}|$  increases through the coupling regime,  $\nu_{QPC}$  subsequently evolves from 2 to

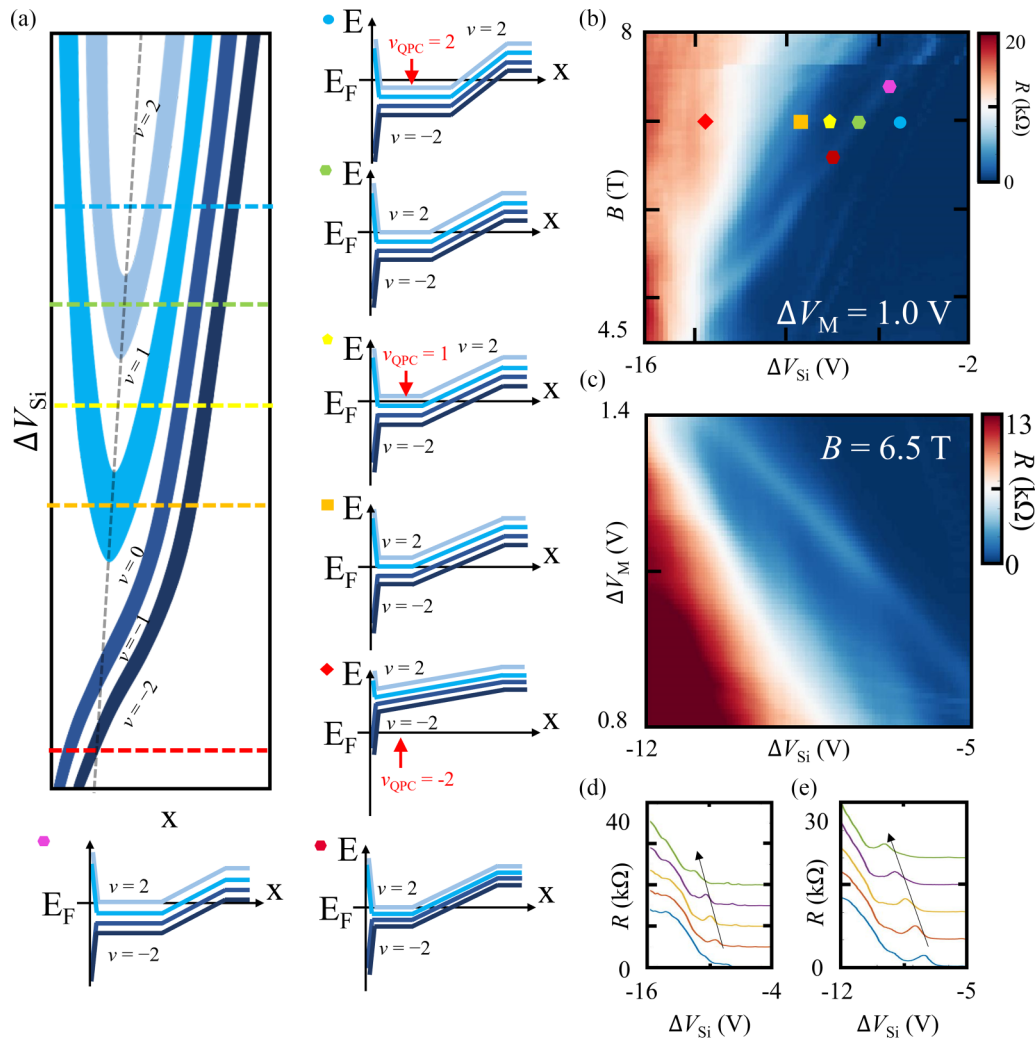


FIG. 3. Selective manipulation of quantum Hall states at *pnp* configuration. (a) Schematics of the evolution of spatial distribution (denoted by coordinate  $x$  along the width of QPC) of QH states in the QPC channel as  $V_{Si}$  is tuned. At certain  $V_{Si}$  values, counterpropagating compressible strips (of the same Landau index) at the opposite channel boundaries are brought into equilibrium at the center of the channel (color dashed line), while its corresponding Landau level brought to Fermi energy (energy-band diagram with corresponding color marks). This leads to backscattering of the selected QH state, giving rise to (b) resistance peaks observed in the measured four-probe resistance as a function of  $\Delta V_{Si}$  and magnetic field  $B$  (at constant  $\Delta V_M = 1.0$  V). (c) Measured resistance as a function of both dual-bottom gates at  $B = 6.5$  T. (d) Line cuts of (b) at different magnetic fields from 5.5 to 6.5 T along the arrow direction. (e) Line cuts of (c) at different  $\Delta V_M$  from 1.10 to 1.30 V along the arrow direction.

1, then to 0 right before the channel width reaches zero [Fig. 3(a)]. Each time a degeneracy-lifted LL in the channel is in resonance (light-green hexagon and orange square markers) with the Fermi energy, a pair of counterpropagating topological compressible strips on the opposite boundaries of QPC combine into a bulk extended compressible state in the center. This results in the backscattering of the state and a peak in the measured resistance. For  $|n_{QPC}|$  slightly lower than the value at which the resistance peak is observed, the two counterpropagating QHES are brought into close proximity (but not merged), with their tunnel coupling and transmission rate continuously tunable, allowing controlled tunneling spectroscopy of QH states. Further increasing  $|n_{QPC}|$  from the peak value eventually fully fills the LL, resulting in the elimination of the QHES from the channel. At the same time, the next pair of counterpropagating QHES is brought closer

towards the center of the channel. We note that the bottom two degeneracy-lifted LL cannot participate in this process due to their *p*-type nature [Fig. 3(a)].

As the  $\nu = 0$  gap (displacement-field induced inversion-symmetry breaking [50]) increases with increasing  $B$ , a lower *p*-type doping level in the backgate region is needed to keep the LL between  $\nu = 1$  and  $\nu = 2$  in resonance with the Fermi level. This leads to the observed peak position shift as a function of  $B$ . The distance in  $|\Delta V_{Si}|$  to the next resistance peak increases dramatically with  $B$ , suggesting the interaction-driven  $\nu = 1$  gap increases with  $B$ .

The  $\nu = 1$  gap [Figs. 3(c) and 3(e)] also increases as  $\Delta V_M$  ( $\Delta V_{Si}$ ) trend towards increasingly negative (positive) values, respectively, and *n*-type compressible strips are pushed away from the disordered physical edge (see Supplemental Material, S5) [33]. This demonstrates manipulation over the energy

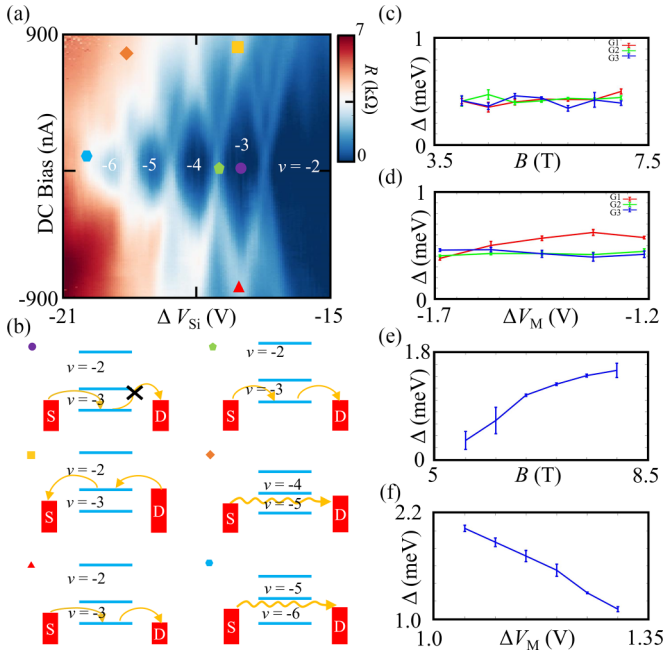


FIG. 4. Characterization of degeneracy-lifted Landau gap via tunable quantum Hall tunneling spectroscopy. (a) Measured resistance as a function of  $\Delta V_{Si}$  and DC bias, and (b) energy-level diagram for typical energy configuration (color mark). Tunnel current between copropagating QH edges brought close at the center of the channel is blocked (allowed) when LL resides out (in) the bias window, leading to zero (finite) lateral resistance of QPC. (c), (d) Extracted energy gap  $\Delta$  at  $\nu = -5$ ,  $\nu = -4$ ,  $\nu = -3$  as a function of electrostatics and magnetic field, measured from  $pp'$  configuration. (e), (f) Extracted energy gap  $\Delta$  at  $\nu = 1$  as a function of electrostatics and magnetic field, measured from  $pp'p$  configuration.

gaps between degeneracy-lifted LL via controlling the proximity of the QHES to the physical boundary.

#### IV. TUNABLE QUANTUM HALL TUNNELING SPECTROSCOPY

Figure 4(a) shows the measured longitudinal resistance as a function of DC bias and  $\Delta V_{Si}$ . An alternating current of 50 nA is applied on top of the DC current bias. By applying a DC bias, the Hall voltage on the two sides of the channel becomes comparable to the energy gaps between degeneracy-lifted LL, which leads to controlled breakdown of the QHES. Similar to the Coulomb blockade (CB) phenomena in a quantum dot [51], the on/off of tunneling current across the 0D region at the center of the channel depends on whether a degeneracy-lifted LL resides within the bias window. When a degeneracy-lifted LL is tuned within the bias window (blue hexagon marker), electrons can tunnel from a QHES on one side of the channel to the other, leading to finite measured resistance. In contrast, when no LL resides in the bias window, the tunnel current is blocked (similar to the CB) and the QHES on the two sides of the channel are effectively decoupled, leading to zero longitudinal resistance. (Also see Supplemental Material, S4 for more details [33].)

The aforementioned tunneling spectroscopy of QHES in the channel is a direct and accurate measurement of energy gaps between degeneracy-lifted LL [52] without relying on variable temperature [53]. At zero bias, the blockade is achieved (purple circle) unless a LL is in resonance with the source-drain chemical potential (green pentagon). As the bias size increases, the range of  $\Delta V_{Si}$  that satisfies the CB condition (corresponding to an energy range at which no LL can be found in the bias window) decreases by the size of bias applied. When the bias window is the same size as the energy gap, the CB is lifted, and finite longitudinal resistance is expected for all  $\Delta V_{Si}$ .

Along the high-resistance ‘‘Coulomb diamond’’ boundary, the DC bias and  $\Delta V_{Si}$  are changing linearly to keep the energy gap and source-drain chemical potential the same. The measured resistance of cotunneling states is 0.45 k $\Omega$ , and the backgate effect in terms of energy can be characterized as 0.403 meV/V (see Supplemental Material, S3) [33]. The energy gap  $\Delta$  of between broken-symmetry QHES is characterized at different magnetic and electrostatic fields [Figs. 4(c)–4(f)] (see Supplemental Material, S7) [33]. A relatively constant gap size is observed for  $\nu = -5$ ,  $-4$ ,  $-3$  [Figs. 4(c) and 4(d)], while the  $\nu = 1$  gap [Figs. 4(e) and 4(f)] is found to increase with increasing  $B$  when QHES are electrostatically displaced from the physical edge. This is consistent with the previous measurements in this work.

#### V. SUMMARY

In summary, we have presented a hybrid-edge and dual-gated QPC with carefully-engineered L-shaped electrostatics. We demonstrate precise manipulation over the emergence, position, and evolution of broken-symmetry QHES, and selective control over their transmission and hybridization. By facilitating controlled quantum tunneling between QHES in a way similar to the CB phenomena, we accurately characterize and tune the symmetry-broken LL gaps with local electrostatic, magnetic fields, and proximity to disorder. Our work provides an approach for improved manipulation and characterization of quantum states with low underlying energy and/or spatial separation, such as fractional quantum Hall states and moiré correlated states. This will allow us to work towards more advanced quantum devices utilizing their exotic physical properties.

#### ACKNOWLEDGMENTS

This work was supported by NSF DMREF Award No. 1922165. The development of the nanostructure and atomically-flat gates are supported by NSF CAREER Award NSF-1944498. Nanofabrication was conducted in the Minnesota Nano Center, which is supported by the National Science Foundation through the National Nano Coordinated Infrastructure Network, Award No. NNCI -1542202. K.W. and T.T. acknowledge support from the JSPS KAKENHI (Grants No. 20H00354, No. 21H05233, and No. 23H02052) and World Premier International Research Center Initiative (WPI), MEXT, Japan.

- [1] Y. Zheng and T. Ando, Hall conductivity of a two-dimensional graphite system, *Phys. Rev. B* **65**, 245420 (2002).
- [2] K. S. Novoselov, A. K. Geim, S. V. Morozov, D. Jiang, M. I. Katsnelson, I. V. Grigorieva, S. V. Dubonos, and A. A. Firsov, Two-dimensional gas of massless dirac fermions in graphene, *Nature (London)* **438**, 197 (2005).
- [3] V. P. Gusynin and S. G. Sharapov, Unconventional integer quantum Hall effect in graphene, *Phys. Rev. Lett.* **95**, 146801 (2005).
- [4] Z. Jiang, Y. Zhang, Y.-W. Tan, H. L. Stormer, and P. Kim, Quantum Hall effect in graphene, *Solid State Commun.* **143**, 14 (2007).
- [5] K. S. Novoselov, Z. Jiang, Y. Zhang, S. V. Morozov, H. L. Stormer, U. Zeitler, J. C. Maan, G. S. Boebinger, P. Kim, and A. K. Geim, Room-temperature quantum Hall effect in graphene, *Science* **315**, 1379 (2007).
- [6] Y.-T. Cui *et al.*, Unconventional correlation between quantum Hall transport quantization and bulk state filling in gated graphene devices, *Phys. Rev. Lett.* **117**, 186601 (2016).
- [7] Y. Zhang, Z. Jiang, J. P. Small, M. S. Purewal, Y.-W. Tan, M. Fazlollahi, J. D. Chudow, J. A. Jaszczak, H. L. Stormer, and P. Kim, Landau-level splitting in graphene in high magnetic fields, *Phys. Rev. Lett.* **96**, 136806 (2006).
- [8] K. Nomura and A. H. MacDonald, Quantum Hall ferromagnetism in graphene, *Phys. Rev. Lett.* **96**, 256602 (2006).
- [9] M. O. Goerbig, R. Moessner, and B. Douçot, Electron interactions in graphene in a strong magnetic field, *Phys. Rev. B* **74**, 161407(R) (2006).
- [10] J. Alicea and M. P. A. Fisher, Graphene integer quantum Hall effect in the ferromagnetic and paramagnetic regimes, *Phys. Rev. B* **74**, 075422 (2006).
- [11] D. A. Abanin, P. A. Lee, and L. S. Levitov, Spin-filtered edge states and quantum Hall effect in graphene, *Phys. Rev. Lett.* **96**, 176803 (2006).
- [12] K. Yang, S. Das Sarma, and A. H. MacDonald, Collective modes and skyrmion excitations in graphene  $SU(4)$  quantum Hall ferromagnets, *Phys. Rev. B* **74**, 075423 (2006).
- [13] V. P. Gusynin, V. A. Miransky, S. G. Sharapov, and I. A. Shovkovy, Excitonic gap, phase transition, and quantum Hall effect in graphene, *Phys. Rev. B* **74**, 195429 (2006).
- [14] I. F. Herbut, Theory of integer quantum Hall effect in graphene, *Phys. Rev. B* **75**, 165411 (2007).
- [15] K. Yang, Spontaneous symmetry breaking and quantum Hall effect in graphene, *Solid State Commun.* **143**, 27 (2007).
- [16] Z. Jiang, Y. Zhang, H. L. Stormer, and P. Kim, Quantum Hall states near the charge-neutral Dirac point in graphene, *Phys. Rev. Lett.* **99**, 106802 (2007).
- [17] A. F. Young, C. R. Dean, L. Wang, H. Ren, P. Cadden-Zimansky, K. Watanabe, T. Taniguchi, J. Hone, K. L. Shepard, and P. Kim, Spin and valley quantum Hall ferromagnetism in graphene, *Nat. Phys.* **8**, 550 (2012).
- [18] S. Kim, J. Schwenk, D. Walkup, Y. Zeng, F. Ghahari, S. T. Le, M. R. Slot, J. Berwanger, S. R. Blankenship, K. Watanabe, T. Taniguchi, F. J. Giessibl, N. B. Zhitenev, C. R. Dean, and J. A. Stroscio, Edge channels of broken-symmetry quantum Hall states in graphene visualized by atomic force microscopy, *Nat. Commun.* **12**, 2852 (2021).
- [19] D. S. Wei, T. van der Sar, J. D. Sanchez-Yamagishi, K. Watanabe, T. Taniguchi, P. Jarillo-Herrero, B. I. Halperin, and A. Yacoby, Mach-Zehnder interferometry using spin- and valley-polarized quantum Hall edge states in graphene, *Sci. Adv.* **3**, e1700600 (2017).
- [20] M. Jo, P. Brasseur, A. Assouline, G. Fleury, H.-S. Sim, K. Watanabe, T. Taniguchi, W. Dummerpanich, P. Roche, D. C. Glatli, N. Kumada, F. D. Parmentier, and P. Roulleau, Quantum Hall valley splitters and a tunable Mach-Zehnder interferometer in graphene, *Phys. Rev. Lett.* **126**, 146803 (2021).
- [21] B. A. Bernevig and S.-C. Zhang, Quantum spin Hall effect, *Phys. Rev. Lett.* **96**, 106802 (2006).
- [22] C. L. Kane and E. J. Mele, Quantum spin Hall effect in graphene, *Phys. Rev. Lett.* **95**, 226801 (2005).
- [23] J. Balakrishnan, G. Koon, A. Avsar, Y. Ho, J. H. Lee, M. Jaiswal, S.-J. Baeck, J.-H. Ahn, A. Ferreira, M. A. Cazalilla *et al.*, Giant spin Hall effect in graphene grown by chemical vapour deposition, *Nat. Commun.* **5**, 4748 (2014).
- [24] A. F. Young, J. D. Sanchez-Yamagishi, B. Hunt, S. H. Choi, K. Watanabe, T. Taniguchi, R. C. Ashoori, and P. Jarillo-Herrero, Tunable symmetry breaking and helical edge transport in a graphene quantum spin Hall state, *Nature (London)* **505**, 528 (2014).
- [25] F. Amet, J. R. Williams, K. Watanabe, T. Taniguchi, and D. Goldhaber-Gordon, Selective equilibration of spin-polarized quantum Hall edge states in graphene, *Phys. Rev. Lett.* **112**, 196601 (2014).
- [26] S. Nakaharai, J. R. Williams, and C. M. Marcus, Gate-defined graphene quantum point contact in the quantum Hall regime, *Phys. Rev. Lett.* **107**, 036602 (2011).
- [27] L. Veyrat, A. Jordan, K. Zimmermann, F. Gay, K. Watanabe, T. Taniguchi, H. Sellier, and B. Saccépé, Low-magnetic-field regime of a gate-defined constriction in high-mobility graphene, *Nano Lett.* **19**, 635 (2019).
- [28] N. F. Ahmad *et al.*, Effect of gap width on electron transport through quantum point contact in hBN/Graphene/hBN in the quantum Hall regime, *Appl. Phys. Lett.* **114**, 023101 (2019).
- [29] K. Zimmermann, A. Jordan, F. Gay, K. Watanabe, T. Taniguchi, Z. Han, V. Bouchiat, H. Sellier, and B. Saccépé, Tunable transmission of quantum Hall edge channels with full degeneracy lifting in split-gated graphene devices, *Nat. Commun.* **8**, 14983 (2017).
- [30] C. Déprez, L. Veyrat, H. Vignaud, G. Nayak, K. Watanabe, T. Taniguchi, F. Gay, H. Sellier, and B. Saccépé, A tunable Fabry-Pérot quantum Hall interferometer in graphene, *Nat. Nanotechnol.* **16**, 555 (2021).
- [31] L. A. Cohen, N. L. Samuelson, T. Wang, K. Klocke, C. C. Reeves, T. Taniguchi, K. Watanabe, S. Vijay, M. P. Zaletel, and A. F. Young, Tunable fractional quantum Hall point contacts in graphene via local anodic oxidation of graphite gates, [arXiv:2204.10296](https://arxiv.org/abs/2204.10296).
- [32] Y. Ronen, T. Werkmeister, D. H. Najafabadi, A. T. Pierce, L. E. Anderson, Y. J. Shin, S. Y. Lee, Y. H. Lee, B. Johnson, K. Watanabe, T. Taniguchi, A. Yacoby, and P. Kim, Aharonov-Bohm effect in graphene-based Fabry-Pérot quantum Hall interferometers, *Nat. Nanotechnol.* **16**, 563 (2021).
- [33] See Supplemental Material at <http://link.aps.org/supplemental/10.1103/PhysRevB.108.245423> for more details, which includes Refs. [34–47].
- [34] A. K. Geim, Graphene: Status and prospects, *Science* **324**, 1530 (2009).
- [35] L. Wang, I. Meric, P. Y. Huang, Q. Gao, Y. Gao, H. Tran, T. Taniguchi, K. Watanabe, L. M. Campos, D. A. Muller, J. Guo, P.

- Kim, J. Hone, K. L. Shepard, and C. R. Dean, One-dimensional electrical contact to a two-dimensional material, *Science* **342**, 614 (2013).
- [36] A. K. Geim and I. V. Grigorieva, Van der Waals heterostructures, *Nature (London)* **499**, 419 (2013).
- [37] C. R. Dean, A. F. Young, I. Meric, C. Lee, L. Wang, S. Sorgenfrei, K. Watanabe, T. Taniguchi, P. Kim, and K. L. Shepard, Boron nitride substrates for high-quality graphene electronics, *Nat. Nanotechnol.* **5**, 722 (2010).
- [38] G. Eber, K. von Klitzing, K. Ploog, and G. Weinmann, Two-dimensional magneto-quantum transport on GaAs-Al<sub>x</sub>Ga<sub>1-x</sub>As heterostructures under non-ohmic conditions, *J. Phys. C: Solid State Phys.* **16**, 5441 (1983).
- [39] V. Tsemekhman, K. Tsemekhman, C. Wexler, J. H. Han, and D. J. Thouless, Theory of the breakdown of the quantum Hall effect, *Phys. Rev. B* **55**, R10201 (1997).
- [40] G. Nachtwei, Breakdown of the quantum Hall effect, *Physica E* **4**, 79 (1999).
- [41] V. Singh and M. M. Deshmukh, Nonequilibrium breakdown of quantum Hall state in graphene, *Phys. Rev. B* **80**, 081404(R) (2009).
- [42] A. M. R. Baker, J. A. Alexander-Webber, T. Altbacumer, and R. J. Nicholas, Energy relaxation for hot Dirac fermions in graphene and breakdown of the quantum Hall effect, *Phys. Rev. B* **85**, 115403 (2012).
- [43] C. Dillard, X. Lin, M. A. Kastner, L. N. Pfeiffer, and K. W. West, Breakdown of the integer and fractional quantum Hall states in a quantum point contact, *Physica E* **47**, 290 (2013).
- [44] S. Tian, P. Wang, X. Liu, J. Zhu, H. Fu, T. Taniguchi, K. Watanabe, J.-H. Chen, and X. Lin, Nonlinear transport of graphene in the quantum Hall regime, *2D Mater.* **4**, 015003 (2016).
- [45] P. Haremski, M. Mausser, A. Gauß, K. von Klitzing, and J. Weis, Electrically induced breakdown of the quantum Hall effect at different Hall bar widths: Visualizing the edge- and bulk-dominated regimes within a quantum Hall plateau, *Phys. Rev. B* **102**, 205306 (2020).
- [46] S. Kim, J. Nah, I. Jo, D. Shahrjerdi, L. Colombo, Z. Yao, E. Tutuc, and S. K. Banerjee, Realization of a high mobility dual-gated graphene field-effect transistor with Al<sub>2</sub>O<sub>3</sub> dielectric, *Appl. Phys. Lett.* **94**, 062107 (2009).
- [47] N. W. Ashcroft and N. D. Mermin, *Solid State Physics* (Cengage Learning, Boston, Massachusetts, 2022).
- [48] B. Özyilmaz, P. Jarillo-Herrero, D. Efetov, D. A. Abanin, L. S. Levitov, and P. Kim, Electronic transport and quantum Hall effect in bipolar graphene *p-n-p* junctions, *Phys. Rev. Lett.* **99**, 166804 (2007).
- [49] J. Velasco Jr, G. Liu, W. Bao, and C. N. Lau, Electrical transport in high-quality graphene *pnp* junctions, *New J. Phys.* **11**, 095008 (2009).
- [50] A. J. M. Giesbers, L. A. Ponomarenko, K. S. Novoselov, A. K. Geim, M. I. Katsnelson, J. C. Maan, and U. Zeitler, Gap opening in the zeroth Landau level of graphene, *Phys. Rev. B* **80**, 201403(R) (2009).
- [51] C. W. J. Beenakker, Theory of Coulomb-blockade oscillations in the conductance of a quantum dot, *Phys. Rev. B* **44**, 1646 (1991).
- [52] K. Wang, A. Harzheim, T. Taniguchi, K. Watanabe, J. U. Lee, and P. Kim, Tunneling spectroscopy of quantum Hall states in bilayer graphene *p-n* junctions, *Phys. Rev. Lett.* **122**, 146801 (2019).
- [53] A. J. M. Giesbers, U. Zeitler, M. I. Katsnelson, L. A. Ponomarenko, T. M. Mohiuddin, and J. C. Maan, Quantum-Hall activation gaps in graphene, *Phys. Rev. Lett.* **99**, 206803 (2007).